Atmos. Chem. Phys. Discuss., 11, 24591–24629, 2011
www.atmos-chem-phys-discuss.net/11/24591/2011/
doi:10.5194/acpd-11-24591-2011

Atmospheric Chemistry and Physics Discussions

Airborne hyperspectral surface and cloud bi-directional reflectivity observations in the Arctic using a commercial, digital camera

A. Ehrlich[1], E. Bierwirth[1], M. Wendisch[1], A. Herber[3], and J.-F. Gayet[4]

[1]Leipzig Institute for Meteorology (LIM), University of Leipzig, Leipzig, Germany
[3]Alfred Wegener Institute for Polar and Marine Research (AWI), Potsdam, Germany
[4]Laboratoire de Météorologie Physique (LAMP), Université Blaise Pascal, Aubière Cedex, France

Received: 27 June 2011 – Accepted: 19 July 2011 – Published: 1 September 2011

Correspondence to: A. Ehrlich (a.ehrlich@uni-leipzig.de)

Published by Copernicus Publications on behalf of the European Geosciences Union.

Abstract

Spectral radiance measurements by a digital single-lens reflex camera were used to derive the bi-directional reflectivity of clouds and different surfaces in the Arctic. The camera has been calibrated radiometrically and spectrally to provide accurate radiance measurements with high angular resolution. A comparison with spectral radiance measurements with the SMART-Albedometer showed an agreement within the uncertainties of both instruments. The bi-directional reflectivity in terms of the hemispherical directional reflectance factor HDRF was obtained for sea ice, ice free ocean and clouds. The sea ice, with an albedo of $\rho = 0.96$, showed an almost isotropic HDRF, while sun glint was observed for the ocean HDRF ($\rho = 0.12$). For the cloud observations with $\rho = 0.62$, the fog bow – a backscatter feature typically for scattering by liquid water droplets – was covered by the camera. For measurements above a heterogeneous stratocumulus clouds, the required number of images to obtain a mean HDRF which clearly exhibits the fog bow has been estimated with about 50 images (10 min flight time). A representation of the HDRF as function of the scattering angle only reduces the image number to about 10 (2 min flight time).

The measured cloud and ocean HDRF have been compared to radiative transfer simulations. The ocean HDRF simulated with the observed surface wind speed of 9 m s^{-1} agreed best with the measurements. For the cloud HDRF, the best agreement was obtained by a broad and weak fog bow simulated with a cloud droplet effective radius of $R_{\text{eff}} = 4$ µm. This value agrees with the particle sizes from in situ measurements and retrieved from the spectral radiance of the SMART-Albedometer.

1 Introduction

Surface reflectivity is a key parameter to estimate the Earth's atmosphere energy budget. As lower boundary condition, it is a parameter controlling the solar radiative transfer in the atmosphere. Considering the directional nature of radiometric quantities,

ACPD
11, 24591–24629, 2011

e.g. radiance, the bi-directional reflectivity distribution function (BRDF) fully describes the surface characteristics (e.g. Nicodemus et al., 1977; Schaepman-Strub et al., 2006). For the application of spaceborne instruments based on measurements of solar radiation, the BRDF is critical to retrieve aerosol or cloud properties. Hyer et al. (2011) found that correcting the surface albedo in the aerosol retrieval of the Moderate Resolution Imaging Spectroradiometer (MODIS) significantly reduces the variability of the bias between MODIS and ground based AOD measurements.

The BRDF of clouds is required to estimate their impact on the Earth's energy budget from spaceborne measurements. Satellite instruments primarily measure spectral radiance and mostly do not cover the entire hemisphere. However, the energy budget is calculated by hemispheric irradiance. To convert the satellite observations of reflected radiance into hemispheric upward irradiance, cloud BRDF models are needed. Plane-parallel radiative transfer calculations are not sufficient to simulate BRDF of inhomogeneous clouds (e.g. Loeb and Davies, 1997; Varnai and Marshak, 2007). Analyzing observations of the Earth Radiation Budget Satellite (ERBS), Loeb and Davies (1997) found that plane-parallel simulations underestimate the reflectivity in the backscattering direction. Varnai and Marshak (2007) observed a bias in the cloud optical thickness retrieved by MODIS, which depends on the viewing angle of the sensor and cloud inhomogeneity. Both effects are significant for viewing angles about 60° and larger.

Several ground-based and airborne retrieval techniques have been developed to derive the BRDF of different surfaces and clouds. While local ground-based measurements provide BRDF for characteristic homogeneous surfaces (e.g. von Schönermark et al., 2004; Dumont et al., 2010), airborne data cover a larger measurement area and average over a mixture of different surface types, which is more suitable to the pixel size of spaceborne observations.

State-of-the-art airborne BRDF instruments are mostly based on a scanning system measuring spectral radiance in different viewing angles. The Cloud Absorption Radiometer (CAR) presented by Gatebe et al. (2005) utilizes a radiance optical inlet with a 1° field of view that is rotated with 100 r min^{-1}. An entire scan of the lower hemisphere

ACPD
11, 24591–24629, 2011

is obtained within 2–3 min. From CAR BRDF, measurements above ocean, savanna, salt pans, snow, and clouds are reported (Gatebe et al., 2003; Lyapustin et al., 2010).

A similar instrument including polarimetric data, the Research Scanning Polarimeter (RSP), is used by Litvinov et al. (2011) to validate BRDF models of vegetation and soil surfaces. The RSP employs a telescope with 0.8° field of view and a double mirror with a scan rate of about 70 r min^{-1} to scan an area of 120°.

Here we present airborne BRDF measurements using a commercial, digital single-lens reflex camera. Its high spatial resolution allows to measure with an angular resolution of about 0.1°. Such type of camera is still rarely applied in atmospheric sciences, while there is an increasing use in vegetation and soil monitoring (Lebourgeois et al., 2008). Only a few studies used such camera measurements quantitatively. From radiance-calibrated conventional photographs, Cox and Munk (1954) derived a parametrization of ocean BRDF. Digital cameras have been introduced in the last century for ground based cloud cover detection (e.g. Long et al., 2006; Schade et al., 2009). However, radiance-uncalibrated signals of the camera sensor have been used to detect clouds by analyzing the three RGB (red, green, blue) spectral channels of the CCD (charged coupled device) sensor.

We analyze radiance-calibrated digital camera images obtained from airborne measurements performed during a campaign in the Arctic. They are introduced in Sect. 2. The procession of the digital camera images including radiometric and spectral calibration is shown in Sect. 3. BRDF measurements for different surfaces are presented in Sect. 4. For the cloud and ocean BRDF, the results are discussed and compared to radiative transfer simulation in Sect. 5. Section 6 presents the conclusions of this paper.

2 Instrumentation and measurements

We report on data collected during the Solar Radiation and Phase discrimination of Arctic Clouds (SORPIC) campaign in May 2010. During SORPIC the Polar 5 aircraft,

ACPD
11, 24591–24629, 2011

owned by the Alfred Wegener Institute for Polar and Marine Research (AWI), Bremerhaven, Germany, was employed to investigate Arctic clouds with a set of remote sensing and in situ instruments. With the Polar 5 based in Longyearbyen at Svalbard (78° 13′ N, 15° 38′ E), in total 13 flights have been conducted covering the area of the Greenland sea west of Svalbard.

The major purpose of the flights was to quantify the horizontal and vertical distribution of ice and liquid water in mixed-phase clouds using different independent approaches, including remote sensing and in situ measurements. The airborne instrumentation for remote sensing included the Spectral Modular Airborne Radiation measurement sysTem (SMART-Albedometer), the hyperspectral camera system AISA Eagle, the Airborne Mobile Aerosol Lidar (AMALi), and a commercial CANON EOS-1D Mark III digital camera. Additionally, an airborne sun photometer was operated to characterize aerosol properties. For in situ measurements, a Nevzorov probe, the Polar Nephelometer, a Cloud Particle Imager (CPI), and the Particle Measuring System (PMS) Forward Scattering Spectrometer Probe (FSSP-100) were installed on Polar 5. A detailed description of the instrumentation is given by Lampert et al. (2009) and Gayet et al. (2009). For sea ice measurements, the electromagnetic-induction (EM) system EM-bird was operated in a towed sonde during the flights on 13 and 14 May 2010 (Haas et al., 2009).

To demonstrate the potential of BRDF measurements with the CANON camera, we present three selected cases of measurements above clouds, sea ice, and open water. For the cloud case we focus on observations of pure liquid water clouds, observed on 17 May 2010 south of Svalbard over ice free sea. A strong advection of warm air produced a persistent cloud layer in the lower boundary layer, with cloud top increasing from south to north from 200 m to 700 m. Measurements above sea ice and open water were obtained during a flight with clear sky conditions on 14 May 2010. The sea ice was observed at about 82° N, 2° W, the open water at about 79° 20′ N, 10° E. In all cases clear sky was reported above the aircraft.

ACPD
11, 24591–24629, 2011

3 Digital camera

3.1 General characteristics

The CANON EOS-1D Mark III is a digital single lens reflex (DSLR) camera and incorporates a CMOS (Complementary Metal Oxide Semiconductor) image sensor that provides three spectral channels (RGB). The advantage of the CMOS image sensor compared to CCD sensors is the possibility of using larger sensors with low power consumption. This allows pixels with larger surface area, which increases the dynamic range of the sensor. With the new sensor generation, the noise and dark current level of CMOS sensors have been reduced to typical values of CCD sensors (Kaufmann, 2010).

The CMOS sensor applied in the CANON EOS-1D Mark III has the Advanced Photo System APS-H format with a 28.1 mm × 18.7 mm sensor area (crop factor of 1.3). The sensor has a 3908 × 2600 pixel grid and covers in total about 10.2×10^6 pixels (10 megapixels).

To cover a large area, the camera was configured with the wide-angle lens Canon EF 14mm f/2.8L II USM. The camera field of view Θ is calculated from the lens focal length of $f = 14$ mm and the sensor chip size d:

$$\Theta = 2 \cdot \arctan\left(\frac{d}{2f}\right). \quad (1)$$

For the horizontal ($d = 28.1$ mm) and vertical ($d = 18.7$ mm) direction, the angle of view is $\Theta = 90.2^\circ$ and $\Theta = 67.5^\circ$, respectively. The image diagonal has an angle of view of $\Theta = 100.6^\circ$. The corresponding angular resolution of each pixel is about 0.025°.

The camera was installed on Polar 5 close to a low definition digital video camera as shown in Fig. 1. To protect the camera lens from damage by split and rain water, a glass window was integrated in the aircraft frame in front of the lens. The camera was fixed to the aircraft frame, which made a correction of the aircraft attitude necessary.

ACPD
11, 24591–24629, 2011

To guarantee the overlap of at least two subsequent images, the camera was aligned with its long image side along the aircraft axis.

To obtain the full dynamic range of the camera sensor chip, only raw data (RAW) were analyzed. Compared to the standard JPG format (8 bit), the RAW format provides 16 bit dynamic range. To read the camera manufacturer specific RAW format (Canon RAW version 2, CR2), we employed the open source tool DCRAW (http://www.cybercom.net/~dcoffin/dcraw/). With DCRAW, the CR2 images have been converted into portable pixmap format (PPM) files using the command:

dcraw – c – v – t0 – o0 – r1111 – k0 – S16384 – 4.

To avoid any manipulation of the original measurements, no white balance was applied by setting the multipliers of all channels to 1. The darkness level was set to 0 and the saturation level to 16 384, respectively, with linear interpolation in between. Finally, the dark current of the images was determined in the laboratory for different camera settings and environmental conditions and subtracted from the data.

3.2 Spectral calibration

To compare the camera measurements with spectral measurements of the SMART-Albedometer and radiative transfer simulations, the spectral sensitivity of each RGB channel was determined in the laboratory. The camera was mounted in front of a grating monochromator (Zolix Omni-λ300). A 200 W halogen lamp was used as radiation source. The spectral irradiance emitted by the lamp was determined by cross calibration of a 1000 W halogen lamp traceable to the National Institute of Standards and Technology (NIST) standard. Measurements with the camera were made between 300 nm and 700 nm wavelength for steps of 5 nm. For the monochromator, a grating with a blaze wavelength of 500 nm and a groove density of 1200 mm^{-1} was chosen, providing a spectral resolution of 0.1 nm. The wavelength accuracy of the monochromator is specified with 0.2 nm. The bandwidth was set to 5 nm, providing a sufficiently high radiance to be detected by the camera.

ACPD
11, 24591–24629, 2011

The relative spectral response RSR_λ function is defined by the normalization:

$$\int_0^\infty RSR_\lambda \, d\lambda = 1. \quad (2)$$

It is calculated from the measured camera signal S_λ and the irradiance $F_{l,\lambda}$ emitted by the 200 W halogen lamp by

$$RSR_\lambda = \frac{S(\lambda)}{F_{l,\lambda}} \cdot \left(\int_0^\infty \frac{S(\lambda)}{F_{l,\lambda}} \, d\lambda \right)^{-1}. \quad (3)$$

The RSR_λ function measured in the laboratory is shown in Fig. 2 for all three camera channels. The RSR_λ of all channels is non-Gaussian, with full width of half mean FWHM ranging between 76 nm for the blue channel and 89 nm for the green channel. The center wavelength λ_c of each channel was determined as 591 nm (red, channel 1), 530 nm (green, channel 2), and 446 nm (blue, channel 3).

3.3 Radiometric calibration

The exposure time of the camera, aperture (f-number), and film speed were fixed during the measurements. The settings with an exposure time of 1/2656 s, an f-number of F/9.1, and a film speed of ISO-400 were chosen for cloud and sea ice observations with high reflectivities but worked as well for measurements above the open ocean. The short exposure time was chosen to avoid distortion due to the aircraft movement.

The radiometric calibration was obtained in the laboratory with use of a NIST traceable radiance source (integrating sphere). The camera was mounted in the laboratory together with the glass window required for the aircraft installation (Fig. 1) in front of the aperture of the integrating sphere in 5 cm and 15 cm distance. For both distances the exit port of the integrating sphere with 6 cm diameter did not cover the whole image. Therefore, a series of images was taken while the camera was moved horizontally and vertically. No differences between measurement at both distances were observed. Therefore, all images have been merged into a single calibration.

ACPD
11, 24591–24629, 2011

Figure 3a shows the original calibration coefficients k of the merged images for channel 1 (591 nm). The plot indicates that the raw data of the camera is noisy. The noise is typical for CMOS image sensors and randomly distributed independent on the pixel position, as shown by laboratory tests (not shown here). Compared to channel 1, the noise of channel 3 (446 nm) is of similar magnitude, while channel 2 (530 nm) shows a reduced noise level. This is probably caused by the doubled number of channel 2 pixels of the Bayer filter used in the CMOS sensor. The data analysis is not seriously affected by the noise as it is counterbalanced by the high number of pixels. To remove the noise in the calibration, a 2-dimensional polynomial fit of 4th degree was applied to smooth the data. The final calibration coefficients $\bar{k}$ used to process the data are shown in Fig. 3b for channel 1. It shows that the sensitivity of the CMOS sensor is maximum in the center and decreases towards the edges of the sensor. The difference between maximum and minimum is about 40 %. This vignetting effect is well known for digital cameras (see Lebourgeois et al., 2008 and Olsen et al., 2010). This pattern has been observed in all three channels, indicating that the pattern results from the lens effects.

Lebourgeois et al. (2008) corrected the vignetting effect by fitting a polynomial function onto an average image of about 500 images. This method does not work if the observed surface is a non-isotropic reflector itself, e.g. sea ice, clouds, and open water. For such surfaces, the vignetting effect will be superimposed by the BRDF of the surface. In this case the vignetting effect has to be eliminated by a radiometric calibration as presented above for the CANON camera. The uncertainty in the radiometric calibration is about 6 % for each channel, mainly resulting from the uncertainty given for the certified radiance source.

3.4 Geometry

As the camera is fixed to the aircraft frame, a correction for the aircraft attitude has to be applied before averaging different images. The definition of the coordinate systems is shown in Fig. 4, where the position of the Sun is defined by the solar zenith angle

ACPD
11, 24591–24629, 2011

θ_0 and the solar azimuth angle φ_0. The pixel coordinates are given by the viewing zenith angle θ_v and the viewing azimuth angle φ_v. The viewing zenith angle is derived from Eq. (1) by replacing the diameter of the sensor with the corresponding distance of each pixel to the center of the sensor. The viewing azimuth angle is defined clockwise, with 0° showing into flight direction. θ_v and φ_v have been corrected for the aircraft roll and pitch angle by rotating the pixel coordinates. From this correction, the zenith and azimuth angles of the reflected radiation in Earth fixed coordinates θ_r and φ_r are derived. Additionally, the images have been rotated into the azimuthal direction of the Sun φ_0.

Assuming single scattering, for each image pixel the scattering angle ϑ of direct solar radiation has been calculated. ϑ is defined as the angle between the direction of the Sun and the viewing direction and is calculated by:

$$\vartheta = 180° - \arccos(-\sin\theta_0 \cdot \cos\varphi_0 \cdot \sin\theta_r \cdot \cos\varphi_r - \sin\theta_0 \cdot \sin\varphi_0 \cdot \sin\varphi_r + \cos\theta_0 \cdot \cos\theta_r)$$

3.5 Hemispherical-directional reflectance factor HDRF

The reflectivity of surfaces is generally described by the bi-directional reflectance distribution function BRDF (Nicodemus et al., 1977; Schaepman-Strub et al., 2006). The BRDF describes how the incident irradiance F_i from one direction (θ_i, φ_i) is reflected by a surface or layer (e.g. cloud) into the direction (θ_r, φ_r). Here, $F_i = \cos\theta_i \cdot F_{0,i}$ refers to a horizontal surface. With the reflected radiation being the radiance $I_r(\theta_r, \varphi_r)$, the BRDF in units of sr^{-1} is defined by:

$$\mathrm{BRDF}\ (\theta_i, \varphi_i; \theta_r, \varphi_r) = \frac{dI_r\ (\theta_i, \varphi_i; \theta_r, \varphi_r)}{dF_i\ (\theta_i, \varphi_i)}. \quad (4)$$

In the literature the dimensionless bi-directional reflectance factor BRF is often used instead of BRDF. It is defined as the ratio of the radiance I_r actually reflected by a

ACPD
11, 24591–24629, 2011

sample surface to the radiance $I_{r,L}$ reflected by an ideal (non-absorbing) and diffuse (Lambertian) standard surface for identical irradiation and beam-geometry. An ideal Lambertian surface reflects the radiation isotropically and it holds $\mathrm{BRDF_L} = (\pi\ \mathrm{sr})^{-1}$. With Eq. (4) this equals to:

$$\mathrm{BRF}\ (\theta_i,\ \varphi_i;\ \theta_r,\ \varphi_r)\ =\ \pi\ \mathrm{sr}\cdot\mathrm{BRDF}\ (\theta_i,\ \varphi_i;\ \theta_r,\ \varphi_r). \tag{5}$$

However, both BRDF and BRF can be measured directly only when an artificial radiation source is applied. We present measurements in atmospheric conditions where the surface is illuminated by the Sun ($F_i = F_{dir} = \cos\theta_0 \cdot F_0$, $\theta_i = \theta_0$, $\varphi_i = \varphi_0$) and by diffuse radiation (F_{diff}). Both components give the global irradiance $F_{glob} = F_{dir} + F_{diff}$. In this case, the hemispherical-directional reflectance factor HDRF is measured (Schaepman-Strub et al., 2006):

$$\mathrm{HDRF}(\theta_0,\varphi_0;\theta_r,\varphi_r) = \quad \pi\mathrm{sr}\cdot\frac{\mathrm{d}I_r(\theta_0,\varphi_0;\theta_r,\varphi_r)}{\mathrm{d}F_{glob}(\theta_0,\varphi_0)}, \tag{6}$$

$$\begin{aligned} &= f_{dir}\cdot\mathrm{BRF}(\theta_0,\varphi_0;\theta_r,\varphi_r) \\ &+(1-f_{dir})\cdot BRF(2\pi;\theta_r,\varphi_r). \end{aligned} \tag{7}$$

The measured HDRF can be split into the BRF(θ_0, φ_0; θ_r, φ_r) for illumination of the surface by the Sun and the BRF(2π; θ_r, φ_r) for pure diffuse illumination of the surface. Both components are weighted with $f_{dir} = F_{dir}/(F_{dir} + F_{diff})$, the fraction of direct incident radiation.

4 Measurements

4.1 Spectral radiance

By applying the radiometric calibration, the camera provides spectral radiances for each pixel and camera channel. The accuracy of the calibration has been verified by

ACPD
11, 24591–24629, 2011

comparing the nadir radiance of the camera to spectral measurements of the SMART-Albedometer, which has an uncertainty of 6 % for radiance measurements. The radiance optical inlet of the SMART-Albedometer has a field of view of 2.1°. This spot corresponds to about 16 000 pixels of the camera. For each image these nadir pixels have been averaged. Furthermore, the spectral data of the SMART-Albedometer have been adapted to the camera measurements by convolving the relative spectral response functions of the three camera channels (see Sect. 3.2).

In Fig. 5a, measurements of channel 1 are compared for an exemplary time interval on 17 May 2010 covering different surfaces such as sea ice, open ocean, and clouds. Despite the lower temporal resolution of the camera measurements (one image within 12 s), the radiances obtained from the camera images follow the temporal course of the SMART-Albedometer measurements (temporal resolution of about 1 s). The mean value of the SMART-Albedometer measurements between 09:28 and 10:28 UTC is $\bar{I} = 0.108\,\mathrm{W\,m^{-2}\,nm^{-1}\,sr^{-1}}$, while the camera observed a mean nadir radiance of $\bar{I} = 0.104\,\mathrm{W\,m^{-2}\,nm^{-1}\,sr^{-1}}$. This difference of 4 % mainly resulting from the radiometric calibration ranges in the uncertainties of both instruments. As illustrated by the ratio of both measurements in the lower panel of Fig. 5a, the single data points differ more due to a non-perfect temporal and spatial allocation of the sampled area, which makes averaging necessary. The standard deviation between both data sets is $0.005\,\mathrm{W\,m^{-2}\,nm^{-1}\,sr^{-1}}$ with a correlation coefficient of 0.99 (see Fig. 5b). For the other spectral channels (not shown here), a similar behaviour has been observed, with differences in the mean values of 1 % for channel 2 and 2 % for channel 3. Standard deviation and correlation coefficient are almost identical for all channels. The agreement between both instruments shows that the CANON camera is capable to quantitatively measure the distribution of reflected radiances that can be used to derive the HDRF. As channel 2 shows the lowest deviation to the SMART-Albedometer data and has the lowest electronic noise, as discussed in Sect. 3.3, in the following the results will be shown for channel 2 (530 nm) only.

ACPD
11, 24591–24629, 2011

4.2 HDRF examples

Images of the CANON camera have been analyzed for three cases: sea ice, open water, and clouds. The HDRF was calculated using Eq. (6). The downward irradiance $F_{\mathrm{glob}}(\theta_0, \varphi_0)$ was obtained from measurements of the SMART-Albedometer. The time and position of the observations, the corresponding position of the Sun, and number of images used to build the averaged HDRFs are given in Table 1. The measurements above sea ice and open water were conducted on 14 May. The cloud scene is part of the measurements conducted on 17 May, which have been analyzed above in Sect. 4.1. Using the irradiance measurements of the SMART-Albedometer, we additionally calculated the spectral albedo for each case. The measured albedo corresponding to the 530 nm channel of the camera is given in Table 1. For sea ice the albedo reaches a mean value of $\rho = 0.96$. Above open water and clouds, $\rho = 0.12$ and $\rho = 0.62$, respectively, were observed.

The mean HDRF of each case is shown in Fig. 6 for camera channel 2. Additionally, a single characteristic image of the observed surface is shown.

4.2.1 Sea ice

Similarly to the albedo, the highest HDRF with values exceeding 1.0 was observed for sea ice, which was almost completely covered by snow. The measurements were conducted during the release of the towed EM-bird sonde, which observed a mean sea ice thickness of 2.5 m. Therefore, the rope of the sonde was present in all images, slightly affecting the HDRF measurements. Furthermore, ice ridges as shown in Fig. 6a were frequently observed on the sea ice, showing a high contrast in the reflected radiance between shadow and illuminated areas. These horizontal inhomogeneities remain partly present in the mean HDRF calculated from 46 single images. However, the HDRF shows an almost Lambertain-like pattern with only slight variability between 0.95 and 1.10 in the magnitude of HDRF. The minimum values are observed

ACPD
11, 24591–24629, 2011

for nadir direction. The weak anisotropy with increasing HDRF along the principle plane is slightly stronger in the direction of the Sun (up to 1.1) than in the opposite direction (up to 1.0). For a similar solar zenith angle of $\theta_0 = 67^\circ$, Lyapustin et al. (2010) showed that the hot spot of the Sun influences the measured HDRF for zenith angles higher than 30° along the principle plane. This is in agreement with the camera measurements covering zenith angles up to about 60°.

4.2.2 Sea water

The measurements above sea water show a more pronounced hot spot (sun glint) in the camera measurements. In general, the HDRF of sea water with minimum values of about 0.04 is significantly lower than for the sea ice and cloud cases, which agrees with the low albedo. The hot spot, which was only partly covered by the camera, shows values of up to 0.43. The maximum ranging outside the camera angle of view (specular reflection for 61°) might be even higher. As discussed by Cox and Munk (1954), the hot spot is caused by sun glint at the surface waves, which are visible in the individual camera image of Fig. 6d. The surface wind measured by a drop sonde during the observations had a speed of about 9 m s^{-1} with northerly direction (360°).

Compared to the sea ice and cloud measurements, the open water measurements require less images (11) for averaging because the sea surface is more homogeneous as seen from about 3000 m altitude than for the sea ice and cloud observations.

4.2.3 Clouds

The HDRF of a representative cloud was derived from measurements (50 individual images) above a low level stratus cloud layer. For the area covered by the camera, the cloud HDRF ranges between 0.45 and 0.8 for the area covered by the camera. The anisotropy of the cloud HDRF mainly reflects the anisotropy of the scattering phase function of the cloud particles. For liquid water droplets, the scattering phase function has a maximum in forward scattering direction, which explains the increasing HDRF

ACPD
11, 24591–24629, 2011

in the direction of the Sun. The minimum values in both HDRF and scattering phase function are observed for the broad range of sideways scattering ($\vartheta = 80$–120°), which corresponds to the nadir direction of the camera measurements for solar zenith angle $\theta_0 = 56.5^\circ$. In the backscatter region, the scattering phase function of spherical particles shows local maxima (glory $\vartheta > 175^\circ$ and fog bow $\vartheta \approx 138^\circ$). While the glory was not covered by the camera, the fog bow is visible in the measured HDRF as a ring around the backscatter point ($\theta_r = \theta_0 = 56.5^\circ$).

4.3 Averaging

Due to inhomogeneities of the observed scene, the camera images have to be averaged to obtain a representative HDRF measurement. In the above examples, all available images (46, 11, and 50) have been averaged for the sea ice, open water, and cloud case, respectively. Especially for clouds, the narrow pattern of the glory features including the fog bow are only visible in a single image if the clouds are highly homogeneous. In most cases, even cloud layers such as stratocumulus have small scale inhomogeneities that disturb the view on the glory features. Therefore, averaging of several images is required to remove cloud inhomogeneities in the HDRF measurements.

For a typical stratocumulus observed on 17 May, 09:32 UTC to 09:42 UTC, we investigated how many images are needed for sufficient averaging. A single image illustrating the inhomogeneous horizontal cloud structure of the stratocumulus is shown in Fig. 7. The mean HDRFs for averaging 5, 10, 20, and 50 images are shown in Fig. 8 for channel 2. With a sampling frequency of one image for each 12 s, this corresponds to flight times of 1 min, 2 min, 4 min, and 10 min. The plots show that for averaging 5 and 10 images, the cloud structure is still visible in the mean HDRF. Using more images (20 and 50), the cloud structure begins to vanish. At the same time, the glory feature becomes more pronounced in the mean HDRF. This implies that for the stratocumulus case investigated here, averaging of about 50 images or more is necessary to obtain a HDRF in which the scattering phase function of the cloud droplets dominates the mean

ACPD
11, 24591–24629, 2011

HDRF compared to cloud inhomogeneities.

To quantify the inhomogeneity of the HDRF, the standard deviation σ_{15° of the HDRF was calculated for a circle of zenith angles lower than 15° (about 70 000 camera pixels). This narrow area was chosen to avoid that the standard deviation is affected by the fog bow at zenith angles larger than 15°. Before calculating σ_{15°, the HDRF was filtered by a 2-D low pass filter using an averaging window of 50 × 50 pixels. The filter removes the electronic noise in the images that would also have been reduced by averaging of images and thus biased σ_{15°. The filter window of 50 × 50 pixels is smaller than the natural cloud homogeneities and thus separates the effects of the electronic noise and natural cloud inhomogeneities. The values of σ_{15° calculated for the mean HDRF of 5, 10, 20, and 50 images are given in Table 2. The values decrease with increasing number of images from $\sigma_{15^\circ} = 0.014$ for 5 images to $\sigma_{15^\circ} = 0.009$ for averaging 50 images. In general, σ_{15° does not converge to zero with increasing number of images because the theoretical HDRF is not constant in the 15° circle. To estimate the range of σ_{15° for a perfectly homogeneous cloud, radiative transfer simulations have been performed. For a cloud of optical thickness of $\tau = 12$ and particle effective radius of $R_{\text{eff}} = 10\,\mu\text{m}$, the simulations give a σ_{15° of 0.01. This ideal value ranges above $\sigma_{15^\circ} = 0.009$ obtained for the mean HDRF using 50 images. This contradiction can only be explained by general differences of the measured and simulated HDRF but shows that an average of 50 images is sufficient to eliminate cloud inhomogeneities.

A way to reduce the required number of images is to present the HDRF as function of the scattering angle ϑ. Assuming that the scattering at homogeneous surfaces is rotationally symmetric with respect to the solar zenith angle, each image can be translated from the HDRF (θ_0, φ_0; θ_r, φ_r) defined by the solar and viewing zenith and azimuth angles into a HDRf(ϑ) defined by the scattering angle ϑ. This transformation allows to average several image pixels into one HDRF value for the corresponding ϑ. We calculated HDRF(ϑ) with a resolution of 0.1°. For each incremental scattering angle $\Delta\vartheta = 0.1^\circ$, about 10 000 pixels were averaged. In this way, the electronic noise of the camera sensor and the horizontal cloud inhomogeneities are smoothed more

ACPD
11, 24591–24629, 2011

efficiently. The corresponding mean HDRF(ϑ) for averaging 5, 10, 20, and 50 images are shown in the right panels of Fig. 8 for channel 2. The HDRF(ϑ) shows much less variability due to cloud inhomogeneities compared to the mean HDRF shown in the left panels of Fig. 8. Already for the mean of 5 images, the glory feature can be identified. Averaging 10 images or more, the horizontal cloud inhomogeneities have been removed almost completely.

5 Simulated HDRF

For the measurements above open water and above clouds, the HDRF was simulated by 1-D plane-parallel radiative transfer calculations. The simulations were run with the library for radiative transfer libRadtran by Mayer and Kylling (2005) using the discrete ordinate radiative transfer solver DISORT version 2.0 by Stamnes et al. (1988). The meteorological input (profiles of static air temperature, relative humidity, and static air pressure) was obtained from the drop sound released from Polar 5 at 10:25 UTC, 14 May for the open water case and 09:36 UTC, 17 May for the cloud case.

Radiances have been calculated for the entire lower hemisphere. For one half of the cloud case with viewing direction into the Sun and for the entire open water case, where the HDRF is more homogeneous, the angular resolution was 5° for the azimuth angle and 3° for the zenith angle. The second half of the cloud case including the glory features in the backscattering region were simulated with a higher angular resolution of 0.5° for both angles. The results have been interpolated to the same grid as obtained by the camera measurements to allow a direct comparison.

5.1 Open water

The BRDF of sea water implemented in libRadtran is taken from the parametrization of Cox and Munk (1954) and Nakajima and Tanaka (1983). Mainly the surface wind speed determines the shape of the BRDF and the magnitude of the sun glint and

ACPD
11, 24591–24629, 2011

was adjusted to the measurements during SORPIC. For the pigment concentration ($0.01\,mg\,m^{-3}$) and the salinity (0.1 ppt) default values were considered. To analyze the sensitivity of the simulations with respect to the wind speed, three simulations with $5\,m\,s^{-1}$, $9\,m\,s^{-1}$ and $15\,m\,s^{-1}$ were performed, with $9\,m\,s^{-1}$ being the value measured during the observations by a drop sonde. The wind direction was set to a northerly direction (360°) corresponding to the observations.

The result of the HDRF simulations with $9\,m\,s^{-1}$ wind speed is shown in Fig. 9a. The low values and the position of the sun glint agree with the measurements presented in Fig. 6e. In Fig. 9b the absolute differences between measurements and simulations are given. For most of the areas covered by the camera measurements, the differences range below 0.01 indicated by the turquoise color. Only for the sun glint area at zenith angles larger than 45° do the differences increase significantly and exceed values of −0.2. The negative values show that in this area the simulations overestimate the HDRF compared to the measurements. Unfortunately, the sun glint hot spot is located at the outer edge of the image where measurement uncertainties may increase due to a decreasing sensitivity of the camera sensor towards the sensor edges. However, an improper radiometric calibration of the camera can be excluded as reason of the deviations, as the differences occur only in the hot spot area, while other boundary areas of the image agree well with the simulations.

Alternatively, the angular distribution HDRF(ϑ) can be used to analyze the differences between simulations and measurements as shown in Fig. 9d. The HDRF(ϑ) has been calculated from the simulations in two different ways. The dotted line in Fig. 9d shows the HDRF(ϑ) for the entire hemisphere, while the HDRF(ϑ) plotted as dashed line was calculated only from the area that was covered by the camera images. The significant differences of both methods indicate that the limited field of view covered by the camera has to be considered when comparing the HDRF(ϑ). The simulations of the entire hemisphere are higher for most of the scattering angles because they include the viewing directions close to the horizon, where multiple scattering leads to enhanced reflection. However, comparing simulations and measurements, the simulated HDRF(ϑ)

ACPD
11, 24591–24629, 2011

of the selected area differs for scattering angles lower than 80° from the measurement, while for larger scattering angles they fit into the uncertainty range of the measurements. The position of the local sun glint maximum within the image is well covered by the measurements, but the magnitude differs by up to 0.25.

The HDRF of simulations carried out with surface wind speeds of $5\,m\,s^{-1}$ and $15\,m\,s^{-1}$ are shown in Fig. 9c and e. Compared to the $9\,m\,s^{-1}$ HDRF, it stands out that the maximum of the sun glint area decreases with increasing wind speed. The closest agreement with the measurements is obtained from the simulations with $15\,m\,s^{-1}$ wind speed. However, while the simulations with $9\,m\,s^{-1}$ wind speed fit to the measurements for all scattering angles larger than 80°, the simulated $5\,m\,s^{-1}$ and $15\,m\,s^{-1}$ HDRF differ for these scattering angles. The HDRF using $5\,m\,s^{-1}$ wind speed ranges significantly below the measurements for scattering angles between 12° and 80°, while the $15\,m\,s^{-1}$ HDRF ranges above the measurements for all scattering angles. The higher HDRF values simulated for $15\,m\,s^{-1}$ wind speed may result from an increase of white caps. The amount of white caps, which is correlated to the albedo of open water (Gordon and Jacobs, 1977), increases nearly linearly between $5\,m\,s^{-1}$ and $15\,m\,s^{-1}$ as shown by Stramska and Petelski (2003). A higher albedo is directly linked to a higher HDRF. Therefore, we argue that the measured HDRF correspond best to the observed wind speed of $9\,m\,s^{-1}$, despite the differences in the sun glint area.

5.2 Clouds

To analyze the HDRF measured above clouds, radiative transfer calculations were used to simulate the cloud case observed on 17 May. The cloud optical properties required for the model input have been retrieved from SMART-Albedometer measurements using the method introduced by Nakajima and King (1990). For the flight leg between 09:49 UTC and 09:59 UTC (see Table 1), the mean optical thickness was about $\tau = 11.5$, with the cloud droplet effective radius R_{eff} ranging between 4 µm and 10 µm. The effective radius obtained from the in situ instrumentation about one hour after the remote sensing measurements was about $R_{\mathrm{eff}} = 9$ µm.

ACPD
11, 24591–24629, 2011

Considering the variation of R_{eff}, simulations for two clouds with $R_{\text{eff}} = 4\,\mu\text{m}$ and $R_{\text{eff}} = 10\,\mu\text{m}$ have been performed. As τ and R_{eff} are linked with each other, we adjusted τ to fit the simulated HDRF in nadir direction to the measurements of the SMART-Albedometer. For the cases of $R_{\text{eff}} = 4\,\mu\text{m}$ and $R_{\text{eff}} = 10\,\mu\text{m}$, the cloud optical thickness was scaled to $\tau = 10.5$ and $\tau = 12.0$, respectively. Corresponding to the observed marine clouds, the spectral surface albedo is represented by SMART-Albedometer measurements above sea water obtained for similar conditions during the ASTAR 2007 campaign (Ehrlich et al., 2008). For this cloud case with a moderate cloud optical thickness, the albedo is sufficient to describe the surface reflectivity. The BRDF model of Cox and Munk (1954) has not to be applied because additional simulations have shown no differences between simulations using the albedo or the BRDF.

For both simulations with $R_{\text{eff}} = 4\,\mu\text{m}$ and $R_{\text{eff}} = 10\,\mu\text{m}$, the HDRF is shown in Fig. 10 (upper panels). In both cases, the HDRF is characterized by the hot spot for zenith angles larger than 75° in direction of the Sun and the glory and fog bow in the backscattering region. In nadir direction the lowest HDRF is simulated. The comparison of both simulations indicates that the size of the glory decreases with increasing cloud droplet effective radius. The first order maximum is at 176.3° scattering angle for $R_{\text{eff}} = 4\,\mu\text{m}$ and $\vartheta = 178.4°$ for $R_{\text{eff}} = 10\,\mu\text{m}$, respectively. Similarly, the characteristics of the fog bow change with cloud droplet size. For simulations with larger droplet size, the fog bow is more pronounced and the maximum is at a smaller scattering angle compared to a cloud with small droplets.

The simulations are compared to the HDRF derived from the camera measurements in the middle panels of Fig. 10 where the differences between measurements and simulations are shown. Positive differences (green and orange color) correspond to values measured higher than calculated by the simulations. The blue color indicates negative differences where the measured values range below the simulations.

For both simulations the lowest differences are observed in nadir direction, which results from scaling the optical thickness with regard to the measured nadir radiance. Higher differences up to values of −0.2 are obtained for larger zenith angles. In the

ACPD
11, 24591–24629, 2011

direction of the Sun, these differences are related to the hot spot of enhanced HDRF, which is simulated significantly higher than observed by the camera. In the backscatter region, the differences are related to glory features with maximum differences close to the 180° point at 56° zenith angle. Especially the differences corresponding to the fog bow are striking in the simulations for $R_{\text{eff}} = 10\,\mu\text{m}$. While the fog bow pattern is visible for large droplets, the simulations for the smaller cloud droplets ($R_{\text{eff}} = 4\,\mu\text{m}$) do not significantly differ from the measurement. This indicates that the HDRF measurements can be used to characterize the cloud particle size.

A similar picture is obtained by comparing the angular distribution HDRF(ϑ) of the limited area to the camera measurements as illustrated in the lower panels of Fig. 10. Again, the simulations for $R_{\text{eff}} = 4\,\mu\text{m}$ fit better to the observations than the simulations using $R_{\text{eff}} = 10\,\mu\text{m}$. Especially the signature of the fog bow with a broader and lower maximum is reproduced better if smaller cloud droplets are assumed in the simulations. The narrow and intense fog bow simulated for the larger cloud droplets significantly exceeds the measured HDRF(ϑ) at scattering angles around 142°.

The differences at small and large scattering angles below 80° and above 150° correspond to the margins of the camera images where the statistics are bad compared to the center of the images. Furthermore, 3-D effects may reduce the measured HDRF(ϑ) compared to the simulations. As Loeb and Coakley Jr. (1998) and Loeb et al. (1998) have shown, the 3-D structure of clouds leads to a decreasing cloud reflectivity towards the horizon compared to 1-D plane-parallel simulations which we applied here.

6 Conclusions

Images measured with a commercial digital single lens reflex camera have been analyzed to produce surface and cloud HDRF. For this purpose, the camera was calibrated spectrally and radiometrically. The center of the three spectral channels are at 591 nm (red), 530 nm (green), and 446 nm (blue) wavelength with FWHM of about 80 nm. The radiometric calibration showed a decreasing sensitivity towards the boundaries of the

ACPD
11, 24591–24629, 2011

camera sensor, which is a typical vignetting effect of digital photo cameras (Lebourgeois et al., 2008). A comparison with spectral radiance measurements provided by the SMART-Albedometer shows differences below the uncertainty range of both instruments. This agreement shows that the CANON camera is capable to measure calibrated radiances.

HDRF measurements are obtained for sea ice, open water, and clouds. In general the results agree with known literature. Compared to traditional measurements, the high spatial resolution of the camera provides a detailed view on the angular pattern of the HDRF, including the hot spot in the direction of the Sun and the glory features for the cloud HDRF. However, due to the high spatial resolution, averaging is necessary to obtain a representative HDRF if the observed scene is inhomogeneous. For inhomogeneous stratocumulus clouds, the required number of images was estimated at 50. If the HDRF is translated into an angular distribution HDRF(ϑ), the required number of images is reduced to 10. With a sampling frequency of one image per 12 s, this corresponds to sampling times of 10 min and 2 min, respectively. This can be reduced if the maximum sampling frequency provided by the camera (one image in 6 s) is applied. Also, the flight altitude will alter the details resolved by the camera and thus the sampling time for one HDRF measurement.

It has to be pointed out that the HDRF presented here refers to surface characteristics as observed from flight altitude and for atmospheric illumination conditions, including direct solar and diffuse radiation. To obtain the more general surface BRDF, an atmospheric correction has to be applied, which is not done here but planned for future studies. However, for the measurements above open water and clouds, radiative transfer simulations providing HDRF have been applied and compared to the measurements. Except for the sun glint region, the open water case agreed well with the HDRF based on the BRDF parametrization of Cox and Munk (1954). The magnitude of the hot spot caused by sun glint was simulated with higher values compared to the measurements. Simulations with a higher surface wind speed reduced the hot spot but also increased the HDRF outside the hot spot. Further measurements with differ-

ACPD
11, 24591–24629, 2011

ent surface wind conditions and solar zenith angles have to be analyzed to determine whether these differences are model- or measurement-based.

The measurements above clouds showed that the backscatter glory features can be extracted from the images. The position, magnitude, and width of the fog bow agreed with simulations assuming cloud droplets with an effective diameter $R_{\text{eff}} = 4\,\mu\text{m}$. Simulations assuming $R_{\text{eff}} = 10\,\mu\text{m}$ failed to reproduce the observed fog bow. This indicated that the analysis of the fog bow might be used to retrieve the cloud effective diameter. A similar approach was successfully applied by Mayer et al. (2004) who derived the particle size from analyzing the width of the backscatter glory. For ice clouds, multi-angle satellite measurements have been utilized by Chepfer et al. (2002) to retrieve the ice crystal shape. This method, based on differences in scattering phase functions of ice crystals, might be applied to our camera measurements in future studies. However, detailed analysis of the images and further observation of different clouds are necessary to obtain a reliable retrieval. Uncertainties in the aircraft attitude may broaden the fog bow when the images are not perfectly corrected. This would lead to an underestimation of the cloud droplet size. However, HDRF above different clouds (not shown here) did show a more narrow fog bow, indicating larger cloud droplets. As it was not our intention to provide a retrieval method for the cloud effective radius, no detailed studies are shown here.

The HDRF measurements presented here are limited to the field of view of the camera lens, with a maximum of 100° in the image diagonal. Circular flight pattern might be used to increase the angular coverage of the images. However, considering the required averaging, several circles have to be flown, which increases the sampling time of one HDRF measurement significantly. An alternative to improve the camera measurements is the application of a 180° field of view lens, enabling us to cover the entire lower hemisphere within one single image. In this way the full hot spot of the sun and the entire backscatter glory would be covered and therefore provide more detailed information on the surface and cloud microphysical properties.

ACPD
11, 24591–24629, 2011

Acknowledgements. This research was funded by the German Research Foundation (DFG, WE 1900/17-1) and AWI, which generously provided flight hours, logistic support, and general access to POLAR 5 for the SORPIC campaign. For the technical support during SORPIC, we want to acknowledge the company Fielax and personally thank Martin Gehrmann of the AWI flight operations department.

References

Chepfer, H., Minnis, P., Young, D., Nguyen, L., and Arduini, R. F.: Estimation of cirrus cloud effective ice crystal shapes using visible reflectances from dual-satellite measurements, J. Geophys. Res., 107, 4730, 2002. 24613

Cox, C. and Munk, W.: Measurement of the roughness of the sea surface from photographs of the sun's glitter, J. Opt. Soc. Am. A, 44, 838–850, 1954. 24594, 24604, 24607, 24610, 24612

Dumont, M., Brissaud, O., Picard, G., Schmitt, B., Gallet, J.-C., and Arnaud, Y.: High-accuracy measurements of snow Bidirectional Reflectance Distribution Function at visible and NIR wavelengths - comparison with modelling results, Atmos. Chem. Phys., 10, 2507–2520, doi:10.5194/acp-10-2507-2010, 2010. 24593

Ehrlich, A., Bierwirth, E., Wendisch, M., Gayet, J.-F., Mioche, G., Lampert, A., and Heintzenberg, J.: Cloud phase identification of Arctic boundary-layer clouds from airborne spectral reflection measurements: test of three approaches, Atmos. Chem. Phys., 8, 7493–7505, doi:10.5194/acp-8-7493-2008, 2008. 24610

Gatebe, C. K., King, M. D., PLatnick, S., Arnold, G. T., Vermote, E. F., and Schmid, B.: Airborne spectral measurements of surface-atmosphere anisotropy for several surfaces and ecosystems over southern Africa, J. Geophys. Res., 108, 8489, 14 pp., doi:10.1029/2002JD002397, 2003. 24594

Gatebe, C. K., King, M. D., Lyapustin, A. I., Arnold, G. T., and Redemann, J.: Airborne spectral measurements of ocean directional reflectance, J. Atmos. Sci., 62, 1072–1092, 2005. 24593

Gayet, J.-F., Mioche, G., Dörnbrack, A., Ehrlich, A., Lampert, A., and Wendisch, M.: Microphysical and optical properties of Arctic mixed-phase clouds. The 9 April 2007 case study., Atmos. Chem. Phys., 9, 6581–6595, doi:10.5194/acp-9-6581-2009, 2009. 24595

ACPD

11, 24591–24629, 2011

Gordon, H. R. and Jacobs, M. M.: Albedo of Ocean-atmosphere System – Influence of Sea Foam, Appl. Optics, 16, 2257–2260, 1977. 24609
Haas, C., Lobach, J., Hendricks, S., Rabenstein, L., and Pfaffling, A.: Helicopter-borne measurements of sea ice thickness, using a small and lightweight, digital EM system, J. Appl. Geophys., 67, 234–241, doi:10.1016/j.jappgeo.2008.05.005, 2009. 24595
Hyer, E. J., Reid, J. S., and Zhang, J.: An over-land aerosol optical depth data set for data assimilation by filtering, correction, and aggregation of MODIS Collection 5 optical depth retrievals, Atmos. Meas. Tech., 4, 379–408, doi:10.5194/amt-4-379-2011, 2011. 24593
Kaufmann, K.: CMOS Technology for Scientific Imaging, Spectroscopy, 25, 20–25, 2010. 24596
Lampert, A., Ehrlich, A., Dörnbrack, A., Jourdan, O., Gayet, J.-F., Mioche, G., Shcherbakov, V., Ritter, C., and Wendisch, M.: Microphysical and radiative characterization of a subvisible midlevel Arctic ice cloud by airborne observations - a case study, Atmos. Chem. Phys., 9, 2647–2661, doi:10.5194/acp-9-2647-2009, 2009. 24595
Lebourgeois, V., Bégué, A., Labbé, S., Mallavan, B., Prévot, L., and Roux, B.: Can commercial digital cameras be used as multispectral sensors? A crop monitoring test, Sensors, 8, 7300–7322, doi:10.3390/s8117300, 2008. 24594, 24599, 24612
Litvinov, P., Hasekamp, O., and Cairns, B.: Models for surface reflection of radiance and polarized radiance: Comparison with airborne multi-angle photopolarimetric measurements and implications for modeling top-of-atmosphere measurements, Remote Sens. Environ., 115, 781–792, doi:10.1016/j.rse.2010.11.005, 2011. 24594
Loeb, N. and Coakley Jr., J.: Inference of marine stratus cloud optical depths from satellite measurements: Does 1D theory apply?, J. Climate, 11, 215–233, 1998. 24611
Loeb, N. and Davies, R.: Angular dependence of observed reflectances: A comparison with plane parallel theory, J. Geophys. Res., 102, 6865–6881, 1997. 24593
Loeb, N., Varnai, T., and Winker, D.: Influence of subpixel-scale cloud-top structure of reflectances from overcast stratiform cloud layers, J. Atmos. Sci., 55, 2960–2973, 1998. 24611
Long, C. N., Sabburg, J. M., Calbo, J., and Pages, D.: Retrieving cloud characteristics from ground-based daytime color all-sky images, J. Atmos. Ocean. Tech., 23, 633–652, 2006. 24594
Lyapustin, A., Gatebe, C. K., Kahn, R., Brandt, R., Redemann, J., Russell, P., King, M. D., Pedersen, C. A., Gerland, S., Poudyal, R., Marshak, A., Wang, Y., Schaaf, C., Hall, D., and Kokhanovsky, A.: Analysis of snow bidirectional reflectance from ARCTAS Spring-2008

ACPD
11, 24591–24629, 2011

Campaign, Atmos. Chem. Phys., 10, 4359–4375, doi:10.5194/acp-10-4359-2010, 2010. 24594, 24604
Mayer, B. and Kylling, A.: Technical note: The libRadtran software package for radiative transfer calculations – description and examples of use, Atmos. Chem. Phys., 5, 1855–1877, doi:10.5194/acp-5-1855-2005, 2005. 24607
Mayer, B., Schröder, M., Preusker, R., and Schüller, L.: Remote sensing of water cloud droplet size distributions using the backscatter glory: a case study, Atmos. Chem. Phys., 4, 1255–1263, doi:10.5194/acp-4-1255-2004, 2004. 24613
Nakajima, T. and King, M.: Determination of the optical thickness and effective particle radius of clouds from reflected solar radiation measurements, Part I: Theory, J. Atmos. Sci., 47, 1878–1893, 1990. 24609
Nakajima, T. and Tanaka, M.: Effect of wind-generated waves on the transfer of solar radiation in the atmosphere-ocean system, J. Quant. Spectrosc. Ra., 29, 521–537, 1983. 24607
Nicodemus, F., Richmond, J., Hsia, J., Ginsber, I. W., and Limperis, T.: Geometrical Considerations and Nomenclature for Reflectance, vol. 160 of NBS Monograph, US Department of Commerce, National Bureau of Standards, Washington, DC, 1977. 24593, 24600
Olsen, D., Dou, C., Zhang, X., Hu, L., Kim, H., and Hildum, E.: Radiometric Calibration for AgCam, Remote Sens., 2, 467–477, doi:10.3390/rs2020464, 2010. 24599
Schade, N. H., Macke, A., Sandmann, H., and Stick, C.: Total and partial cloud amount detection during summer 2005 at Westerland (Sylt, Germany), Atmos. Chem. Phys., 9, 1143–1150, doi:10.5194/acp-9-1143-2009, 2009. 24594
Schaepman-Strub, G., Schaepman, M. E., Painter, T. H., Dangel, S., and Martonchik, J. V.: Reflectance quantities in optical remote sensing-definitions and case studies, Remote Sens. Environ., 103, 27–42, 2006. 24593, 24600, 24601
Stamnes, K., Tsay, S., Wiscombe, W., and Jayaweera, K.: A numerically stable algorithm for discrete-ordinate-method radiative transfer in multiple scattering and emitting layered media, Appl. Optics, 27, 2502–2509, 1988. 24607
Stramska, M. and Petelski, T.: Observations of oceanic whitecaps in the north polar waters of the Atlantic, J. Geophys. Res.-Oceans, 108, 3086, doi:10.1029/2002JC001321, 2003. 24609
Varnai, T. and Marshak, A.: View angle dependence of cloud optical thicknesses retrieved by Moderate Resolution Imaging Spectroradiometer (MODIS), J. Geophys. Res.-Atmos., 112, D06203, doi:10.1029/2005JD006912, 2007.

ACPD
11, 24591–24629, 2011

von Schönermark, M., Geiger, B., and Röser, H.-P.: Reflection Properties of Vegetation and Soil With a BRDF-Data base, vol. 1, Wissenschaft und Technik Verlag, Berlin, 2004. 24593
690 24593

ACPD
11, 24591–24629, 2011

Table 1. BRDF measurements above sea ice, open water, and clouds.

	Date	Time	Location	Altitude	# of Images	θ_0	φ_0	ρ (530 nm)
Sea Ice	14 May	08:21–08:33	82° 00′ N, 2° 00′ W	100 m	46	67.0°	123.0°	0.96
Open Water	14 May	10:21–10:23	79° 20′ N, 10° 00′ E	3050 m	11	61.1°	165.5°	0.12
Clouds	17 May	09:49–09:59	75° 20′ N, 18° 30′ E	3100 m	50	56.5°	166.5°	0.62

ACPD
11, 24591–24629, 2011

Table 2. Standard deviation σ_{15° of the mean HDRF using 5, 10, 20, or 50 images calculated for a circle of zenith angles lower than 15°. Additionally, σ_{15° is given for a plane-parallel cloud of optical thickness $\tau = 12$ and particle effective radius $R_{\text{eff}} = 10\,\mu\text{m}$.

HDRF	5 Images	10 Images	20 Images	50 Images	Simulation
σ_{15°	0.014	0.014	0.010	0.009	0.010

ACPD
11, 24591–24629, 2011

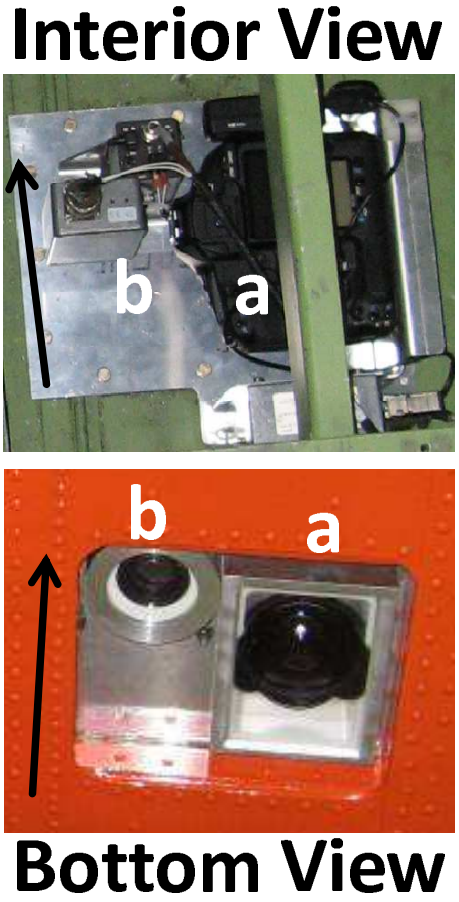

Fig. 1. Photographs of the installation of the CANON camera on board of Polar 5 (arrows indicate the flight direction). In both photographs (interior and bottom view), the CANON camera is labeled **(a)** and the digital video camera **(b)**.

ACPD
11, 24591–24629, 2011

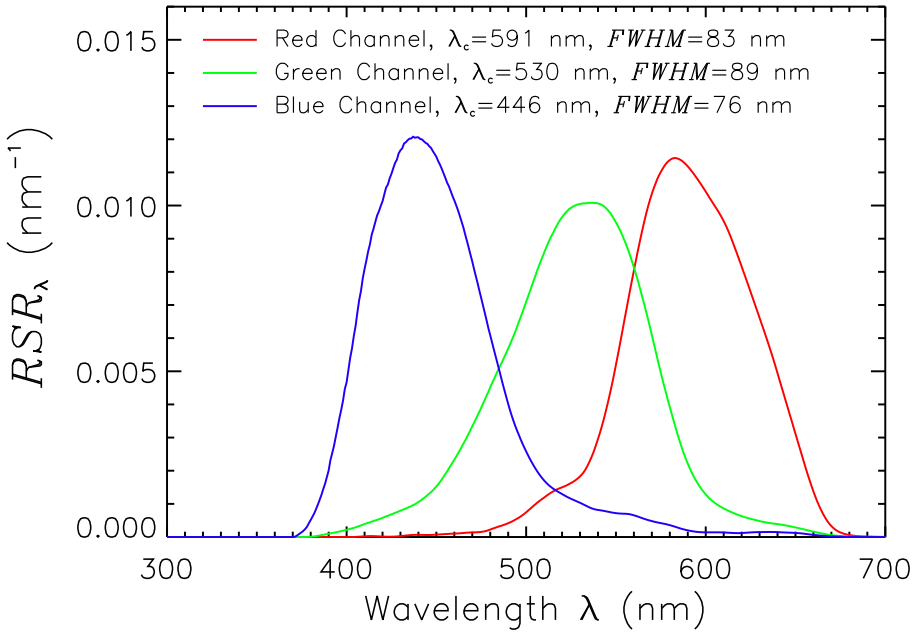

Fig. 2. Relative spectral response function RSR_λ of the three camera channels (red, green, blue). For each channel, the center wavelength λ_c and the FWHM are given.

ACPD
11, 24591–24629, 2011

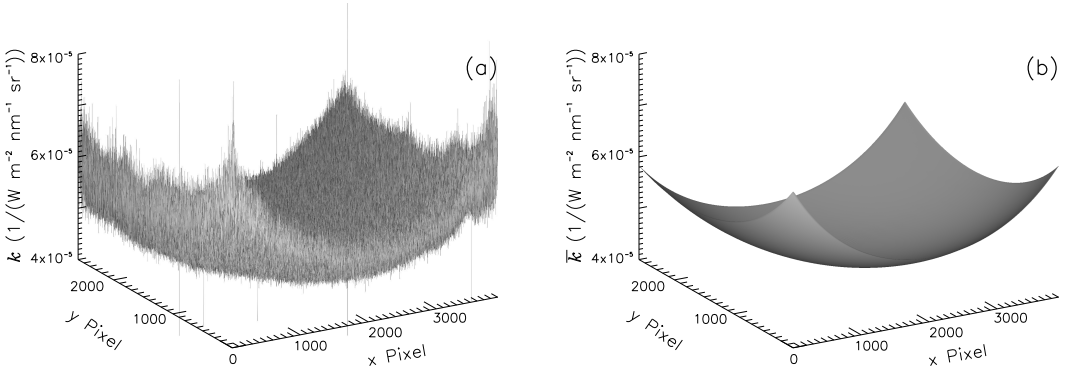

Fig. 3. Radiometric calibration of camera channel 1 ($\lambda = 591$ nm). Panel **(a)** shows the noisy raw data. In Panel **(b)** a 2-D fit was applied to smooth the data. The calibration is valid for an exposure time of 1/2656 s, an f-number of F/9.1, and a film speed of ISO-400.

ACPD
11, 24591–24629, 2011

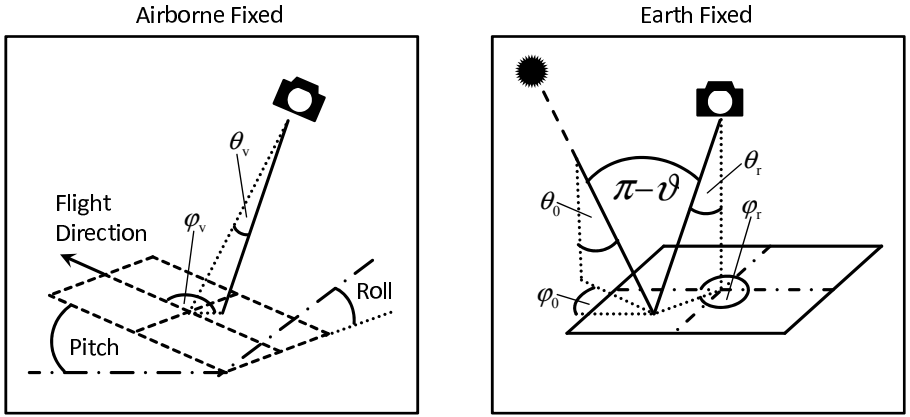

Fig. 4. Illustration of the airborne fixed (left, θ_v, ϕ_v) and Earth fixed coordinates (right, θ_r, φ_r) of one single camera pixel. Additionally, the scattering angle ϑ is indicated with the position of the Sun defined by θ_0, φ_0.

ACPD
11, 24591–24629, 2011

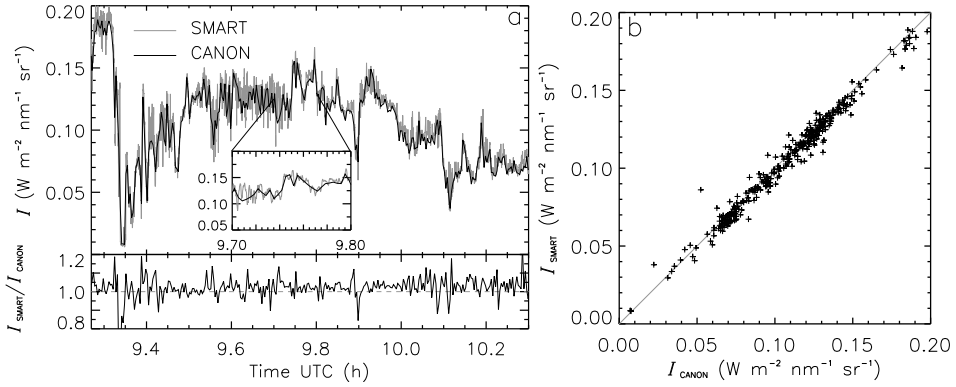

Fig. 5. Time series (17 May 2010) comparison **(a)** of a spectral radiance measured by the SMART-Albedometer (gray) and by the CANON camera (black). Data are shown for the red camera channel ($\lambda = 591$ nm). The correlation between both measurements is illustrated in panel **(b)**.

ACPD
11, 24591–24629, 2011

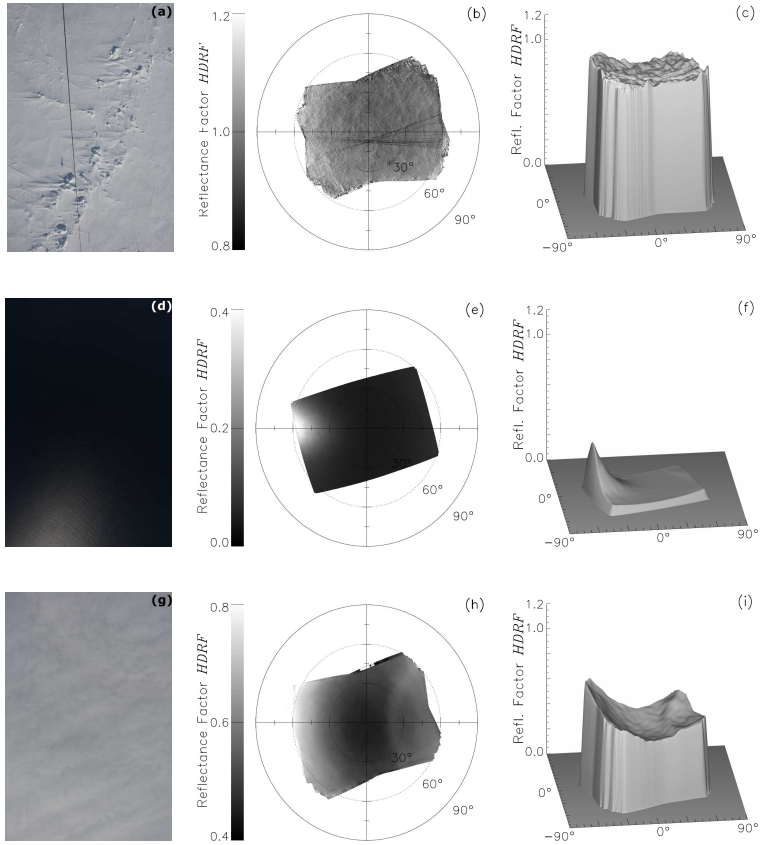

Fig. 6. HDRF measurements with the CANON camera (channel 2) above sea ice (top), open water (center), and clouds (bottom). The left column **(a, d, g)** shows exemplary individual camera images. The averaged HDRF is shown in the center column as polar plot **(b, e, h)** and as smoothed surface in the right column **(c, e, i)**.

ACPD
11, 24591–24629, 2011

Fig. 7. Exemplary single camera image (09:41:23 UTC) of stratocumulus observations used to analyze averaging requirements.

ACPD
11, 24591–24629, 2011

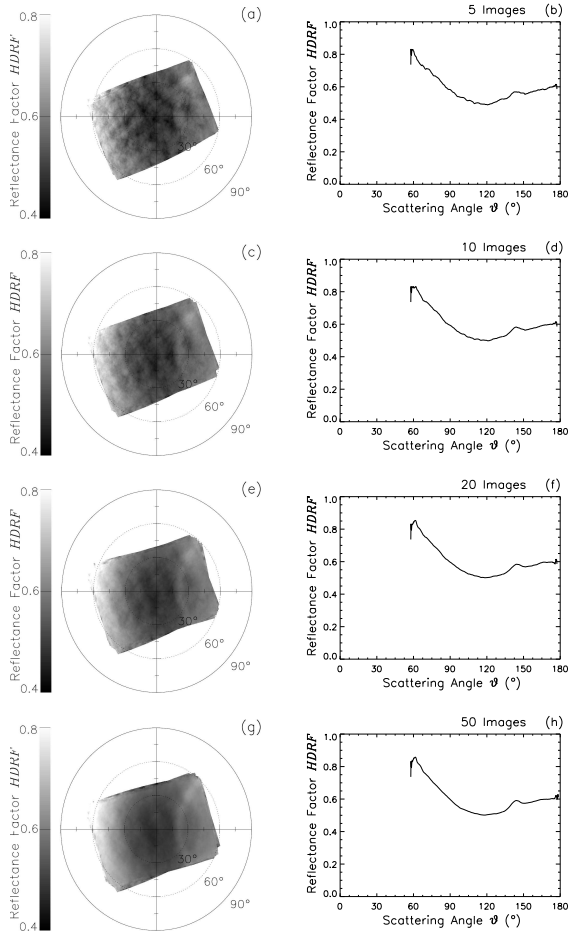

Fig. 8. Average HDRF above clouds (channel 2) calculated from 5, 10, 20, and 50 individual images **(a, c, e, g)**. The right panels **(b, d, f, h)** show the corresponding HDRF(ϑ) as function of the scattering.

ACPD
11, 24591–24629, 2011

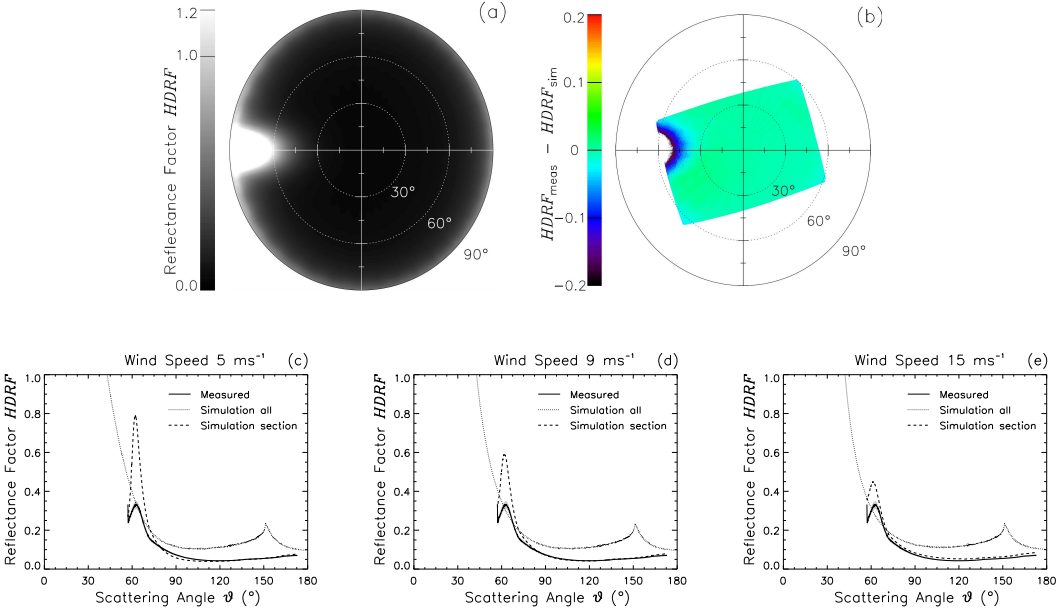

Fig. 9. Simulated HDRF of open water. The upper panels show **(a)** the HDRF simulated with $9\,m\,s^{-1}$ wind speed and **(b)** the difference to the measurements. The angular distribution of the HDRF is compared between measurements (solid line) and simulation with different wind speed in panels **(c)** $5\,m\,s^{-1}$, **(d)** $9\,m\,s^{-1}$, and **(e)** $9\,m\,s^{-1}$. The simulations are shown for the entire hemisphere (dotted line) and only the area covered by the measurements (dashed line). The uncertainty of the measurements is indicated by the gray area.

ACPD
11, 24591–24629, 2011

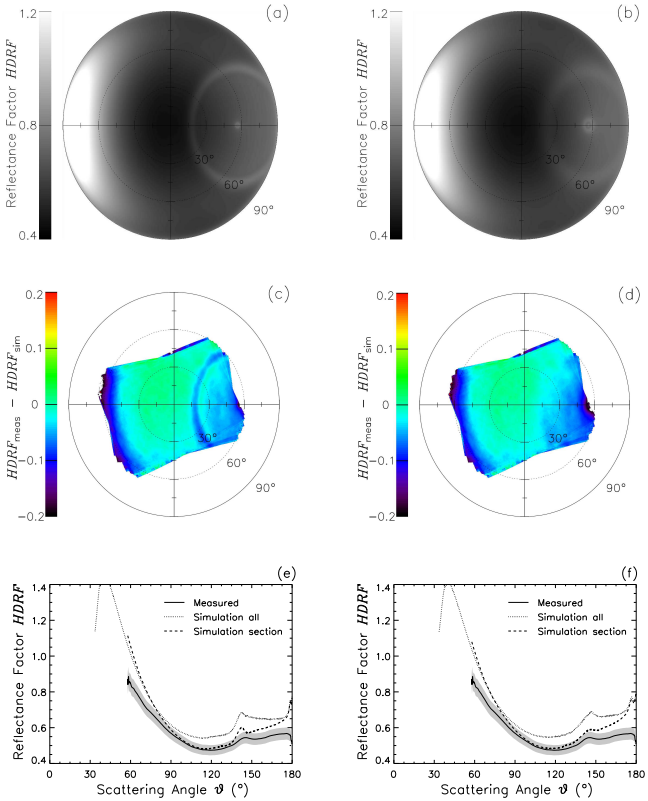

Fig. 10. Simulated HDRF for clouds with optical thickness and effective diameter of $\tau = 12$ and $R_{\text{eff}} = 10\,\mu\text{m}$ (left) and of $\tau = 10$, $R_{\text{eff}} = 4\,\mu\text{m}$ (right). The upper panels show the HDRF of the entire lower hemisphere. Differences between measured and simulated HDRF are given in the middle panels **(c, d)**. The lower panels **(e, f)** give the HDRF(ϑ) as function of the scattering angle for measurements and simulations (entire hemisphere and only area covered by the measurements). The uncertainty of the measurements is indicated by the gray area.

ACPD
11, 24591–24629, 2011